DC to GHz measurements of a Near-Ideal 2D Material: P^{+} Monolayers

Antonio Levy,[1,2] Pradeep Namboodiri,[1] Joshua M. Pomeroy,[1] Xiqiao Wang,[1] Joseph Fox,[1] Richard M. Silver,[1] and Neil M. Zimmerman[1]

[1)] *National Institute of Standards and Technology*

[2)] *Department of Physics and Astronomy, Howard University.*

(*Electronic mail: Neil.Zimmerman@nist.gov)

(Dated: 5 February 2024)

P^{+} monolayers in Si are of great scientific and technological interest, both intrinsically as a material in the "ideal vacuum" of crystalline Si, and because they are showing great promise as qubits of electron and nuclear spin. The GHz complex conductivity $\sigma(\omega)$ can allow one to elucidate basic physical properties and also is important for fast devices, but measuring $\sigma(\omega)$ in 2D materials has not been easy. We report on such measurements, including showing i) qualitatively, a lack of any resonances up to 5 GHz (indicating no energy splittings below about 0.02 meV); and ii) quantitatively ideal Drude behavior of this novel material up to 5 GHz, showing a lower bound on the scattering rate of about $2 \times 10^{10} s^{-1}$. We also discuss deconvolving the confounding effect of the distributed resistance and capacitance of the monolayer.

I. INTRODUCTION

In recent years, workers have developed the ability to generate a subsurface monolayer of P^{+} dopants (typically about ¼ of a full monolayer), surrounded by lattice-matched crystalline Si[1,2]. In addition, the ability to pattern the monolayer with atomic precision using an STM has resulted in an exciting variety of device possibilities, under the rubric of "digital manufacturing"[3] in which nominally the fabrication can be atomically perfect; this variety has resulted in rapid progress in quantum coherent manipulation in both electron and nuclear spin[4,5].

However, some of the basic properties of this novel 2D material are not yet fully understood, including the basic conduction mechanism and energy spectrum . For instance, such a system's conductivity spectrum depends strongly on its energy level spectrum, and thus is a direct reflection of the ground state and excited state physics. The high-frequency conductivity is, in addition, of great importance for the high-speed operation of conventional and quantum devices in this STM-patterned P^{+} monolayer architecture.

In our previous work[6], we proposed a quantitative, non-contact method of sensitively characterizing the GHz response of 2D flakes and showed simulated results on a candidate material. In the present work, we have experimentally demonstrated the applicability of this technique to the important case of a blanket P^{+} monolayer in Si.

The closest previous result to characterization of a blanket P^{+} monolayer embedded in Si in this high-frequency regime is the demonstration of exchange qubits[4] as it includes transmission of signals in "wide" P^{+} lines (10 nm), from which we can surmise qualitatively that some level of GHz transmission was occurring . Our observation of a smooth frequency dependence of the transmission (i.e., no resonances), and ideal Drude behavior in the complex conductivity, adds to our understanding of this 2D material. In the remainder of this publication, we give experimental details of the fabrication, measurement, analysis, show the raw data for transmission and DC resistance and the deduced complex conductivity, and then conclude.

II. EXPERIMENTAL DETAILS

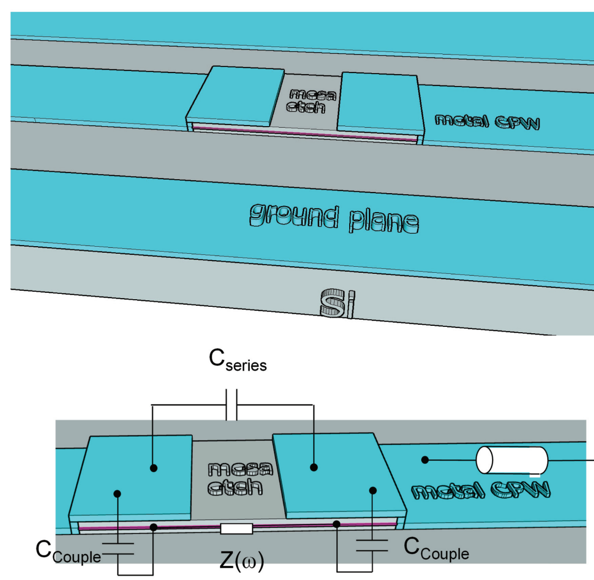

FIG. 1. **Above:** Sketch of the fine area of the gapped CPW device: The purple region is the P^{+} monolayer; grey is Si; teal color is the metal CPW. The gap in the CPW allows us to focus the dominant transmission effect on the μm-sized mesa-etched conducting monolayer. **Below:** sketch with the lumped-parameter circuit elements added.

A. Fabrication

We prepared blanket P^{+} layers using our standard process[7]; briefly (samples W18-F3 and W18-F4) we cleaned atomically-flat Si (001) chips in UHV, exposed the sample to a saturation dose of PH3 gas that resulted in about $\frac{1}{4}$ of a monolayer of P^+, incorporated P atoms substitutionally by heating to 350 °C for two minutes, then overgrew epitaxial Si (33.0 $\pm$ 2.7 nm for W18-F4 and 30.8 $\pm$ 1.6 nm for W18-F3) with a 2 nm room-temperature locking layer. After this, we etched mesas of size (7μm $\times$ 50μm) to a depth of 52 nm , deposited about 185 nm of Al and performed standard photolithography and chemical etching to produce coplanar waveguides (CPWs) (both continuous and with gaps in the center conductor). The continuous CPWs were used to normalize the transmission data to derive the conductivity function.

For series-gapped CPWs, we placed the gap centered over the mesa; see Figure 1 for a sketch of the final device. We note that, as a result of depositing Al over the side of the mesa-etched monolayer, we provided a weak resistive connection R_{contact} between the CPW signal line and the monolayer – in future work, we plan on providing an insulating barrier to avoid this complication. Please see Appendix A for a theoretical analysis of the effect of this resistance.

Finally, we placed the 4 mm $\times$ 10 mm dies into a sample box assembly, wirebonded to Al pads, and mounted the assembly onto the mixing chamber plate of a dilution refrigerator (DR). In this publication, we report measurements taken at the base temperature (thermometer read 10 mK).

We also produced control devices (W22-62 and W22-85) nominally identical with the previous two, with the exception that we did not expose the samples to PH3, and thus they had no P^+. We note that the control samples had a nominally identical overgrown Si layer.

B. Measurement Details

For the high-frequency measurements, we used standard Vector Network Analyzer (VNA) techniques yielding magnitude $|t| = |S_{21}|$ and phase $\phi = \arg(S_{21})$ of the transmission function, with SMA cable assemblies going to the sample box assembly in the DR. The cable assemblies were heat-sunk at all stages using 0 dB attenuators.

To deduce the complex conductivity from $|t|$ and ϕ, we used techniques derived in[6], modified to account for the effects of the distributed impedance in the P^+ monolayer on the capacitive coupling to the signal lines (See Appendix A and Ref.[8] for more details).

For the DC resistance measurement of the sample, we etched Hall bars on the same chips with metalized contact pads on the samples. We made four-point measurements using a closed cycle cryostat at a temperature of 4 K (to suppress parallel conduction in the Si substrate). We then extracted the sheet resistance of the phosphorous monolayer using the geometry of five squares between each of the voltage leads.

III. DATA AND ANALYSIS

Figure 2 shows representative data for the magnitude and phase for transmission t in several structures.

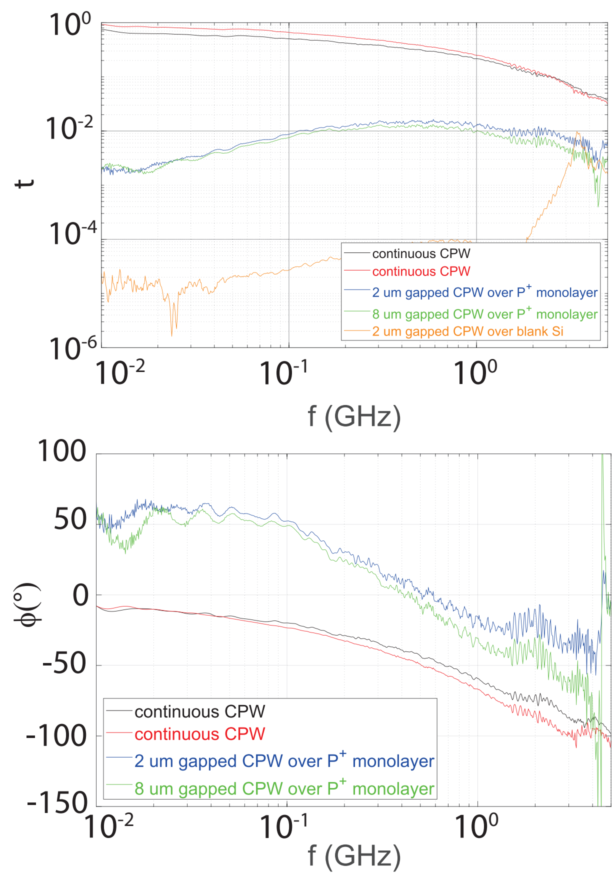

FIG. 2. Raw data for magnitude and phase of transmission coefficient versus frequency. Note the excellent signal dependence on the μm-sized conducting monolayer: i) above the monolayer, the gapped CPW has a much larger transmission than above the undoped Si; ii) the gapped CPW has a much smaller transmission than a continuous CPW. Note also the good reproducibility between the two “continuous CPW” spectra (same cooldown, different wiring) as well as between the two “gapped CPW over P^+ monolayer” (same cooldown, different samples, different wiring). Above about 5 GHz, coupling through the wirebonds removes the difference between monolayer and bare Si (see text). The typical power supplied by the Vector Network Analyzer was -10 to -15 dBm.

Firstly, the two top curves in the upper panel show continuous CPWs (no gap), which demonstrate both the expected low pass filter frequency dependence, good (low) insertion loss below about 1 GHz, and excellent reproducibility (the two measurements were taken on different devices in the same cooldown using different wiring).

Secondly, we note the dynamic range (about a factor of 10^2 or 40 dBm) separating the monolayer transmission data from both the continuous CPW and the CPW with no monolayer. Additionally, the reproducibility shown in sets of data taken on similar configurations (e.g., gapped CPWs) demonstrates the P monolayer is the dominant material being probed. In particular: 1) The transmission in the gapped CPW over undoped Si is about $10^{2.5}$ smaller than in the continuous CPW (power is 10^5 smaller); this shows that the transmission in

5 m of transmission line is totally dominated by the gap of size a few μm. 2) For the dynamic range, we note that the transmission magnitude for the devices with a conducting P^+ monolayer is far larger than the "control" device (no conducting P^+ monolayer) up to about 5 GHz. Above this frequency, the transmission intensity across a series gapped CPW begins to suffer from crosstalk and loses reliability. This qualitative change in the frequency-dependence of the transmission spectrum can be seen in *t* of Fig. 2, which shows that the transmission across the series gapped CPW over undoped Si sharply increases with frequency above approximately 1 GHz, eventually converging to the transmission spectrum across the series gapped CPWs over P^+ mesas, indicating a loss of sensitivity to the P^+ layers. Shortening the wirebond length increased the maximum frequency at which the transmission was dominated by transmission through the series gap between the signal lines. Comparing different samples of the same type, please note the excellent agreement between the two curves with P^+ monolayer, given the two measurements were taken on different devices in same cooldown using different wiring.

Our technique (AC transmission in μm-scale 2D materials using non-contact gapped CPWs) has two main methods of analysis. The first is the qualitative one of looking for resonant features in the transmission. We can see from Figure 2 that, up until the 5 GHz extrinsic limit, we see no such resonant features. Thus, we can conclude that there are no excited states within 0.02 meV of the ground state of the conduction electrons in our P^+ monolayer (see Appendix B for a discussion of the prediction of the Drude model as extended to include possible resonances).

The second method is the quantitative one of deducing the frequency-dependent conductivity $\sigma(\omega)$ from the complex transmission spectrum mathematically. In our previous publication[6], we derived the complex transmission spectrum expected to result from the circuit diagram shown in Fig. 4c:

$$t(\omega) = \frac{2\left[\frac{1}{2Z_{\text{Couple}}+\frac{\alpha}{\sigma(\omega)}} + i\omega C_{\text{Series}}\right]}{2\left[\frac{1}{2Z_{\text{Couple}}+\frac{\alpha}{\sigma(\omega)}} + i\omega C_{\text{Series}}\right] + \frac{1}{Z_{\text{CPW}}}} \tag{1}$$

where Z_{Couple}, the coupling impedance between each signal line and the P^+ monolayer, replaces C_{Couple}. C_{Series} is the capacitive coupling between the signal lines, $\sigma(\omega)$ is the conductivity of the P^+ monolayer, Z_{CPW} is the CPW impedance ($\approx 50\ \Omega$), and α is the ratio of the series gap to the signal line width.

Simply, when the gap in the CPW looks like an open ($\frac{1}{\omega C_{\text{Series}}} >> \left|2Z_{\text{Couple}} + \frac{\alpha}{\sigma(\omega)}\right|$), the signal is transmitted through a series coupling capacitance between the one signal line and the sample of interest, the conductivity of the sample of interest, and capacitive coupling to the second signal line. Since the frequency dependence of the capacitors is smooth and monotonic, features in the sample conductivity vs frequency become detectable.

However, we realized in the course of this work that the simple formula was not sufficient. As discussed in detail in Appendix A, the finite conductivity in the monolayer that forms the capacitor plate leads to a substantial modification in the transmission, and thus we need the result in Appendix A to accurately deduce $\sigma(\omega)$, resulting in:

$$Z_{\text{Couple}} = \frac{\frac{R_{\text{Contact}}}{2}\cosh\left(\sqrt{u}\right) + \frac{l}{w\sigma(\omega)}\frac{\sinh(\sqrt{u})}{\sqrt{u}}}{i\omega C_{\text{Couple}}\frac{R_{\text{Contact}}}{2}\frac{\sinh(\sqrt{u})}{\sqrt{u}} + \cosh\left(\sqrt{u}\right)} \tag{2}$$

Here $u = i\omega C_{\text{Couple}}\frac{l}{w\sigma(\omega)}$, where l and w are the length and width, respectively, of the mesa-etched monolayer underneath both signal lines. The formula in the limit of infinitely large R_{Contact} can be found in Refs.[9] and[10].

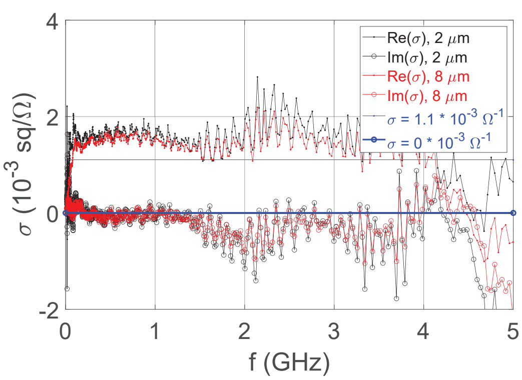

FIG. 3. Complex conductivity deduced from data in Fig. 2, using Equations 1 and 2 and the parameters in Table A1. The two different devices (2 μm and 8 μm gap) were on different dies and were measured in the same cooldown with different wiring. Note that (1.1 $\times$ 10^{-3} sq/Ω is the value of resistance per square measured in the Hall bars.

We have thus taken the complex transmission in Fig. 2 and deduced $\sigma(\omega)$ using Equations 1 and 2, shown in Fig. 3. This deduction requires accurate normalization for the transmission; as discussed in Appendix A, we used the data from the continuous CPW to normalize. We also note that the significant dispersion (dependence on f in Figure 2) arises from the complex impedance of the RC delay embodied in Z_{Couple}; thus, the simple Drude results in Figure 3 are consistent with the dispersion observed in Figure 2.

The values of R_{Contact} used to deduce the conductivity spectra were 138 kΩ and 495 kΩ for the devices with the 2 μm and 8 μm gap, respectively. These values were taken from electronic transport measurements. The values of C_{Couple} were obtained by fitting the transmission spectra between 10 MHz and 100 MHz, where the signal is dominated by the capacitive coupling. It is also worth noting that the values of C_{Couple} used to fit the spectra are close to theoretical expectations.

We note the good reproducibility between the two samples for both real and imaginary parts; the real part of the complex conductivity is about 20% above the DC value measured in Hall bars. We further note that i) $\mathrm{Re}[\sigma(\omega)]$ is frequency-independent, and that ii) $\mathrm{Im}[\sigma(\omega)] \approx 0$ (within the statistical uncertainty). From the discussion in Appendix B , we thus conclude that an upper bound on the scattering time τ is approximately $\frac{0.2}{2\pi(4\mathrm{GHz})} \approx 10$ ps based on the negligible frequency-dependence of the real and imaginary components of $\sigma(\omega)$.

The discrepancy of about 20 % could be due to either i) lateral inhomogeneity in the P^+ monolayer 2D resistance (in some cases, the resistance range across chips is larger than 20 %); ii) a true frequency dependence resulting in a change below about 100 MHz (the lowest frequency we measured with this technique) or iii) the uncertainty of our measurement of t and of the deduction of $\sigma(\omega)$

IV. CONCLUSION

From the qualitative lack of resonances in the raw data in Fig. 2, we can conclude that there are no excited states within about 0.02 meV from the ground state (as expected) [see Appendix B for details]. From the deduced conductivity in Fig. 3, we can see that this nearly-ideal conductor in the "ideal vacuum" of crystalline Si shows behavior identical to the simple Drude model, within the uncertainty. We note the upper bound on the scattering time of $\tau < 10$ ps.

We again note the discrepancy between the real part of the deduced complex conductivity and the DC value measured in Hall bars. As described above, this is likely due to inhomogeneity in monolayer resistivity across a chip. While very unexpected, frequency dependence below 100 MHz cannot be ruled out entirely; we hope to extend one technique or the other to determine the existence of such a dependence.

We can also comment on the strength of our measurement technique in general: While there have been a number of previous techniques to measure GHz conduction in 2D materials (see Ref.[6]), Fig. 3 clearly demonstrates that our technique provides this new capability, with an estimated relative uncertainty $\frac{\delta\sigma(\omega)}{\sigma(\sigma)}$ of at most about 20 %, and provides a wide bandwidth while avoiding the need for Ohmic contact.

In addition to gaining additional scientific information about the P^+ monolayer conducting behavior, our results also bear on the burgeoning use of P^+ qubits and ancillary devices in quantum dots[4]. The natural frequency of the electron spin in a typical magnetic field is of order 10 – 40 GHz, and thus to produce one-qubit rotations and two-qubit coupling requires that the P^+ leads can transmit signals at this frequency range and speed (for pulses). The excellent results obtained recently provide an inference about the ability of the P^+ leads to transmit high-speed signals, and our results provide quantitative confirmation of this inference.

V. ACKNOWLEDGEMENTS

The authors would like to offer thanks to Garnett Bryant, Michael Stewart, Ranjit Kashid, Curt Richter and Albert Rigosi for insightful conversations, and for technical training and assistance throughout this process. We particularly acknowledge Nikolai Zhitenev of NIST for drawing our attention to the effect of the RC delay.

VI. CONFLICT OF INTEREST

The authors declare no conflict of interest.

Appendix A: RC Coupling Derivation

In our previous publication[6] on the theoretical framework for this technique, we assumed a circuit diagram as in Fig. 4, with capacitive coupling to the flake $Z(\omega)$. However, in the present work we realized that much (essentially all) of the frequency dependence of the $t(\omega)$ in Figure 2 is not reflective of intrinsic dispersion in the 2D material P+, but rather arises due to the dispersion of the distributed resistive/capacitive network in the P+.

Thus, in this section, we derive a framework for two modifications mentioned in Fig. 1: i) R_{Contact} as mentioned in the "Fabrication" section and ii) a distributed resistance $R_{\mathrm{Electrode}}$ in the plate of C_{Couple} arising from the non-zero resistivity of the monolayer; both of these modifications can be seen in Figures 4c and 4d. We note that we have chosen to put capacitors at both ends of the distributed RC network[8]; in the limit of large N [see Fig. 4 caption], this boundary condition becomes numerically insignificant.

In the following sections, we will i) recursively derive an expression for Z_N and then ii) approximate $Z_{\mathrm{Couple}} = \lim_{N\to\infty} Z_N$

1. Deriving a General Expression for Z_N

It is clear that R and C decrease in value as N increases. For most of this Section, we will suppress this dependence and simply treat R and C as values that are constant for all elements in the circuit for a given value of N, and then substitute for the decreasing values at the end.

a. Deriving Z_2

It is straightforward to derive

$$Z_2 = \frac{1}{i\omega C + \frac{1}{R + \frac{1}{\frac{2}{R_{\mathrm{Contact}}} + i\omega C}}} \tag{A1}$$

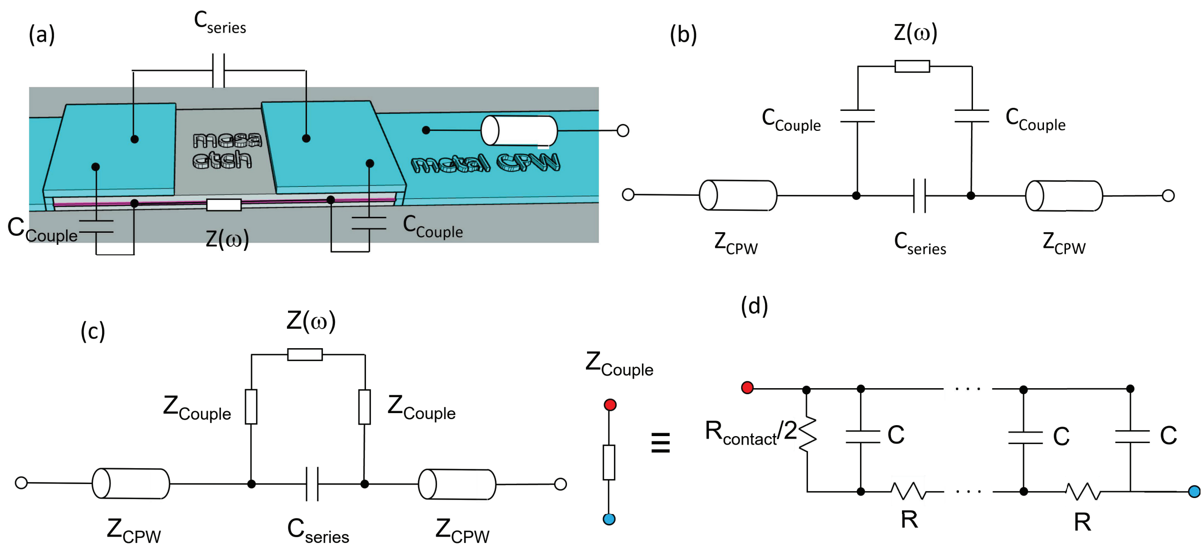

FIG. 4. (a) Magnified portion of Figure 1, with lumped-parameter electrical elements. indicated [corresponding to panel (b)]; (b) Circuit diagram equivalent to our previous publication[6], with simple capacitors C_{Couple}. (c) Modified diagram, where we have replaced C_{Couple} by the more general Z_{Couple}. (d) The details of Z_{Couple}, in particular the R_{Contact} and the distributed RC combination. There are N capacitors and (N – 1) resistors; in the end, we will take the limit as $N \to \infty$.

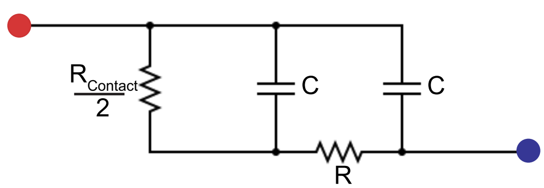

FIG. 5. Circuit for Z_{Couple} for N = 2.

and thus:

$$Z_2 = \frac{\frac{R_{\text{Contact}}}{2}\left(1+i\omega CR\right)+R}{i\omega C\frac{R_{\text{Contact}}}{2}\left(2+i\omega CR\right)+1+i\omega CR} \tag{A2}$$

b. Deriving a General Recursive-Based Relation for Z_N, then Solving for Coefficients

In analogy with Equation A2, in this Subsection we will first show that the trial solution in Equation A2 satisfies the recursion relation and the boundary conditions set by

$$Z_n = \frac{\sum_{m=0}^{N-1}\left(\frac{R_{\text{Contact}}}{2}a_m^N\left(i\omega RC\right)^m + Rb_m^N(i\omega RC)^m\right)}{\sum_{m=0}^{N-1}\left(i\omega C\frac{R_{\text{Contact}}}{2}c_m^N\left(i\omega RC\right)^m + d_m^N\left(i\omega RC\right)^m\right)} \tag{A3}$$

with the constraints that for all coefficients $x \in [a,b,c,d]$, $x_j^i = 0$ whenever $i < 0$ or $i > j-1$. We then solve for the coefficients a, b, c, d. We note, as shown later, that the decreasing nature of the coefficients ensures that the series converge.

We start by observing that

$$Z_{N+1} = \frac{1}{i\omega C + \frac{1}{R+Z_N}} \tag{A4}$$

Now, we will use Equation A2 as a trial solution, and show that it gives a consistent result for Z_{N+1}. Substituting the trial solution from Equation A2 into the recursion relation Equation A3, we obtain:

$$Z_{N+1} = \frac{1}{i\omega C + \frac{1}{R+\frac{\sum_{m=0}^{N-1}\left(\frac{R_{\text{Contact}}}{2}a_m^N(i\omega RC)^m + Rb_m^N(i\omega RC)^m\right)}{\sum_{m=0}^{N-1}\left(i\omega C\frac{R_{\text{Contact}}}{2}c_m^N(i\omega RC)^m + d_m^N(i\omega RC)^m\right)}}} \tag{A5}$$

We can then obtain (the subscript (m-1) arises from the extra capacitor that results in an extra factor of $i\omega C$ in some of the terms)

$$Z_{N+1} = \frac{\sum_{m=0}N\left((\text{ß}\omega RC)^m\left(\frac{R_{\text{Contact}}}{2}\left(a_m^N + c_{m-1}^N\right) + R\left(b_m^N + d_m^N\right)\right)\right)}{\sum_{m=0}^{N}\left((\text{ß}\omega RC)^m\left(i\omega C\frac{R_{\text{Contact}}}{2}\left(c_m^N + a_m^N + c_{m-1}^N\right) + d_m^N + b_{m-1}^N + d_{m-1}^N\right)\right)} \tag{A6}$$

We thus impose the following recursive constraints on the coefficients:

$$a_m^{N+1} = a_m^N + c_{m-1}^N \tag{A7}$$
$$b_m^{N+1} = b_m^N + d_m^N \tag{A8}$$
$$c_m^{N+1} = c_m^N + a_m^N + c_{m-1}^N \tag{A9}$$
$$d_m^{N+1} = d_m^N + b_{m-1}^N + d_{m-1}^N \tag{A10}$$

Substituting these into Equation A6, we obtain:

$$Z_{N+1} = \frac{\sum_{m=0}^{N} \left(\frac{R_{\text{Contact}}}{2} a_m^{N+1} (i\omega RC)^m + R b_m^{N+1}\right)(i\omega RC)^m}{\sum_{m=0}^{N} \left(i\omega C \frac{R_{\text{Contact}}}{2} c_m^{N+1} (i\omega RC)^m + R b_m^{N+1}\right)(i\omega RC)^m} \tag{A11}$$

Note that this is identical with Equation A3, where N has been replaced by N+1. We have thus proven that the trial solution obeys the required recursion relation Equation A4. Next, with the following assignments for N = 2 (see Fig. 5), the trial solution will obey Z_2 in Equation A2: $a_0^2 = 1$, $a_1^2 = 1$, $b_0^2 = 1$, $c_0^2 = 2$, $c_1^2 = 1$, $d_0^2 = 1$, $d_1^2 = 1$, with all other N=2 coefficients being zero. Note that the recursion relations (Equations A7-10) are obeyed fro Z_1 (not shown) and Z_2; thus, in the following we truncate all summations at the known values for N = 2 without loss of generality.

We will now derive recursive equations for the coefficients, and then present useful approximations. Since the solution includes $a_j^i = 0$ whenever i<1, we can obtain $a_0^N = 1$ for all N. It immediately follows from Equation A9 that

$$c_0^N = c_0^{N-1} + a_0^{N-1} \tag{A12}$$
$$= c_0^{N-2} + a_0^{N-2} + a_0^{N-1} \tag{A13}$$
$$= \ldots = c_0^2 + \sum_{k=2}^{N-1} a_0^k = N \tag{A14}$$

Similarly, generalizing to arbitrary m,

$$a_m^N = a_m^{N-1} + c_{m-1}^{N-1} = a_m^2 + \sum_{k=2}^{N-1} c_{m-1}^k \tag{A15}$$

and

$$c_m^N = c_m^{N-1} + a_{m-1}^{N-1} + c_{m-1}^{N-1} = c_m^2 + \sum_{k=2}^{N-1} a_m^k + \sum_{k=2}^{N-1} c_{m-1}^k \tag{A16}$$

Thus, “ratcheting” ourselves upwards, we can see that

$$a_0^N = 1 \tag{A17}$$

$$c_0^N = 1 \tag{A18}$$

$$a_1^N = 1 + \sum_{k=2}^{N-1} k \approx \frac{N^2}{2} \tag{A19}$$

$$c_1^N = 1 + \sum_{k=2}^{N-1} \frac{k^2}{2!} + \sum_{k=2}^{N-1} k \approx \frac{N^3}{3!} \tag{A20}$$

$$a_2^N = \sum_{k=2}^{N-1} \frac{k^3}{3!} \approx \frac{N^4}{4!} \tag{A21}$$

$$c_2^N = \sum_{k=2}^{N-1} \frac{k^4}{4!} + \sum_{k=2}^{N-1} \frac{k^3}{3!} \approx \frac{N^5}{5!} \tag{A22}$$

We thus conclude that the general approximate result is:

$$a_m^N \approx \frac{N^{2m}}{(2m)!} \tag{A23}$$

$$c_m^N \approx \frac{N^{2m+1}}{(2m+1)!} \tag{A24}$$

$$b_m^N \approx \frac{N^{2m+1}}{(2m+1)!} \tag{A25}$$

$$d_m^N \approx \frac{N^{2m}}{(2m)!} \tag{A26}$$

We note that these approximations are good to within approximately 30% for $m < \frac{N}{2}$.

c. Deriving $Z_{\text{Couple}} = \lim_{N\to\infty} Z_N$

As noted earlier, for all coefficients $x \in [a,b,c,d]$, $x_j^j = 0$ whenever $i < 0$ or $i > j-1$ and thus the infinite sums are actually sums from m = 1 to N. However, when we take the limit as $N \to \infty$, we must consider the convergence of the sums, and the appropriateness of using the approximations. In particular, we have confirmed (not shown) that each approximation overstates the actual values of the coefficients; thus, if we can show that the sums converge, this will also show that using the approximations is valid. At a given N, the coefficients peak at m slightly below $\frac{N}{2}$.

Each of the four terms in Equation A2, taking into account the approximations in Equations A23-A26, has the form $\frac{N^{2m}}{(2m)!}(i\omega RC))^m$; ; we now move away from the generic C and R, and instead note that $C = \frac{C_{Couple}}{N}$ and $R = \frac{R_{Electrode}}{N-1}$; we will later expand $R_{Electrode}$ to deduce the desired complex conductivity $\sigma(\omega)$. Noting that both C and R $\propto \frac{1}{N}$, we now see that the four terms, at large N, tend to $\frac{1}{(2m)!}$; thus, the sums have half of the terms of the Taylor expansion for e^1; the sums converge.

We will i) first combine Eqs. A2 and with A23-A26, ii) then replace R and C, taking the limit as $N \to \infty$, and finally iii) simplify Z_{Couple}.

For large N,

$$Z_N = \frac{\sum_{m=0}^{N-1}\left(\frac{R_{\text{Contact}}}{2}\frac{N^{2m}}{(2m)!}(i\omega RC)^m + R\frac{N^{2m+1}}{(2m+1)!}(i\omega RC)^m\right)}{\sum_{m=0}^{N-1}\left(i\omega C\frac{R_{\text{Contact}}}{2}\frac{N^{2m+1}}{(2m+1)!}(i\omega RC)^m + \frac{N^{2m}}{(2m)!}(i\omega RC)^m\right)} \tag{A27}$$

$$Z_N = \frac{\frac{R_{\text{Contact}}}{2}\sum_{m=0}^{N-1}\frac{\left(i\omega R_{\text{Eletrode}}C_{\text{Couple}}\right)^m}{(2m)!} + R_{\text{Electrode}}\sum_{m=0}^{N-1}\frac{\left(i\omega R_{\text{Electrode}}C_{\text{Couple}}\right)^m}{(2m+1)!}}{i\omega C_{\text{Couple}}\frac{R_{\text{Contact}}}{2}\sum_{m=0}^{N-1}\frac{\left(i\omega R_{\text{Electrode}}C_{\text{Couple}}\right)^m}{(2m+1)!} + \sum_{m=0}^{N-1}\frac{\left(i\omega R_{\text{Electrode}}C_{\text{Couple}}\right)^m}{(2m)!}} \tag{A28}$$

We note the Taylor expansions $\cosh(x) = \sum_{m=0}^{\infty}\frac{x^{2m}}{(2m)!}$ and $\sinh(x) = \sum_{m=0}^{\infty}\frac{x^{2m+1}}{(2m+1)!}$ and that $R_{\text{Electrode}} = \frac{l}{w\sigma(\omega)}$, where w is t the electrode's width and l is its length (under the signal line). We obtain:

$$\sum_{m=0}^{\infty}\frac{\left(i\omega\frac{l}{\sigma(\omega)w}C_{\text{Couple}}\right)^m}{(2m+1)!} = \sum_{m=0}^{\infty}\frac{\left(\sqrt{i\omega\frac{l}{\sigma(\omega)w}C_{\text{Couple}}}\right)^{2m+1}}{\sqrt{i\omega\frac{l}{\sigma(\omega)w}C_{\text{Couple}}}(2m+1)!} \tag{A29}$$

$$\sum_{m=0}^{\infty}\frac{\left(i\omega\frac{l}{\sigma(\omega)w}C_{\text{Couple}}\right)^m}{(2m+1)!} = \frac{\sinh\left(\sqrt{i\omega\frac{l}{\sigma(\omega)w}C_{\text{Couple}}}\right)}{\sqrt{i\omega\frac{l}{\sigma(\omega)w}C_{\text{Couple}}}} \tag{A30}$$

Note that the coefficients drop off significantly from the approximations in Equations 23-26 for $m > N/2$; thus, to use the definitions of $\cosh(x)$ and $\sinh(x)$, we take the limit as $N \to \infty$ to obtain:

$$Z_{\text{Couple}}(\omega) = \lim_{N\to\infty} Z_N \tag{A31}$$

$$Z_{\text{Couple}}(\omega) = \frac{\frac{R_{\text{Contact}}}{2}\cosh(\sqrt{u}) + \frac{l}{w\sigma(\omega)}\frac{\sinh(\sqrt{u})}{\sqrt{u}}}{i\omega C_{\text{Couple}}\frac{\sinh(\sqrt{u})}{\sqrt{u}} + \cosh(\sqrt{u})} \tag{A32}$$

where $u = i\omega C_{\text{Couple}}\frac{l}{w\sigma(\omega)}$. In Figure 6, we can see plots of Z_{Couple}, and also comparisons to the simple parallel combination of R_{Contact} and C_{Couple}. The low-frequency limits agree with the parallel configuration, and at higher frequencies, Z_{Couple} is larger than that, due to the interplay of R and C as in Fig. 4(a).

This substantial deviation is what leads us to need to deduce $\sigma(\omega)$ using this much more complicated analysis.

d. Using Z_{Couple} to Analyze Transmission Data

In the main text we combine Equations 1 and 2 to deduce $\sigma(\omega)$). An experimental complication arises from the need for normalization of the transmission data, as otherwise non-idealities in the wiring will substantially degrade this analysis[6]. As shown in Fig. 2, by comparing the "continuous CPW" to the "gapped CPW" data, we can clearly see that the transmission magnitude is dominated by the P+ monolayer; from this observation, we concluded that the best normalization is the continuous CPW data. Thus, when deducing $\sigma(\omega)$ in Fig. 3, for each device we replaced $t(\omega)$ in Equation 1 with $\frac{t_{\text{gapped}}(\omega)}{t_{\text{continuous}}(\omega)}$.

Finally, we wish to compare our technique to the closest previous one[8]. In the previous work, the authors use a similar circuit as in Fig. 4, in order to deduceσ [not $\sigma(\omega)$] for a MOSCAP. In order to achieve quantitative results, they limited their technique to frequencies such that $1\frac{l}{\sigma w} << \frac{1}{\omega C_{\text{Couple}}}$);

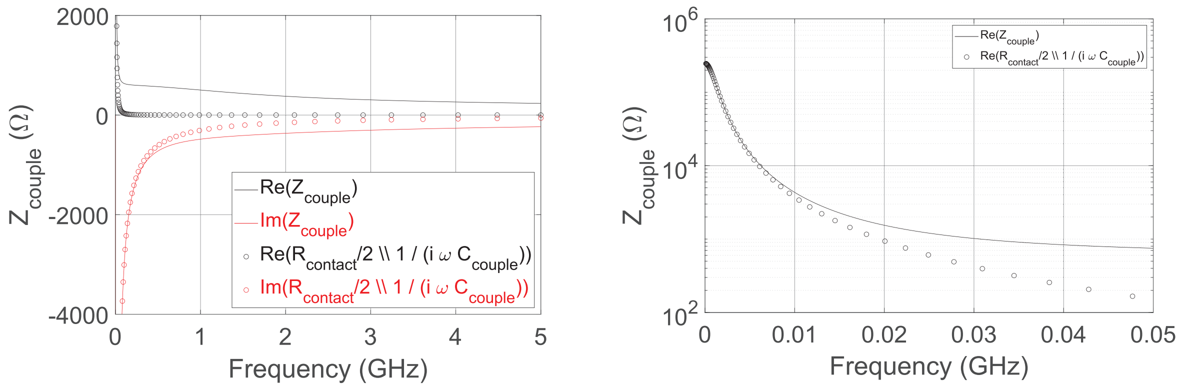

FIG. 6. Theoretical calculation of frequency dependence of Z_{Couple}, from Equation A9, and comparison to the simple parallel combination of R_{Contact} and C_{Couple}. Note the agreement at low frequencies where $\frac{l}{w\sigma} < \frac{1}{\omega C_{\text{Couple}}}$. All parameters are given in Table 1, for the 8 μm gap.

	$2\ \mu m$ gap	$8\ \mu m$ gap
α	2/7	8/7
C_{Couple}	580 fF	510 fF
$\ell\ (\mu m)$	$24\ \mu m$	$21\ \mu m$
R_{Contact}	$138\ k\Omega$	$495\ k\Omega$

TABLE I. Parameters used in deduction of $\sigma(\omega)$. α and l come from the nominal geometry, R_{Contact} from Hall bar measurements, and C_{Couple} from low-frequency measurements where C_{Couple} dominates the transmission[6]. The values of C_{Couple} are within 10% of independent estimates from the nominal geometry.

also, they did not solve for the equivalent impedance, and thus could not deduce the frequency dependence. In contrast, in this work we solve for the impedance (Equation A32), do not limit ourselves in frequency, and deduce the frequency dependence.

Appendix B: Drude Model and Resonances

The Drude model (no resonances) result for the complex conductivity is

$$\sigma(\omega) = \frac{\sigma(0)}{1 - i\omega\tau} \tag{B1}$$

where $\sigma(0) = \frac{ne^2\tau}{m}$ for simple metals, $i = \sqrt{-1}$, and where τ is the scattering time.

Note that $\sigma(\omega)$ will vary from the low-frequency limit (flat Real part and zero Imaginary part) by about 20% when $\omega\tau \approx 0.2$ (see Fig. 7); we can thus put an upper bound on the scattering time of $\tau < 10ps$.

An extension of this model in the case of resonances can be derived as follows:

The dielectric response for multiple resonances is[11]

$$\varepsilon(\omega) = \sum_j \frac{\lambda_j}{\omega_{0,j}^2 - \omega^2 - i\omega/\tau_j} \tag{B2}$$

where λ_j, $\omega_{0,j}$, and τ_j are respectively the weights, center frequencies and lifetimes of the various resonances.

In addition, we can convert $\sigma(\omega) = \frac{\omega}{4\pi i}\varepsilon(\omega)$[12], using the second convention, and with the understanding that in our experiment, the measured transmission corresponds to the conductivity $\sigma(\omega)$ arising from all (bound and free) electrons.

This finally yields

$$\sigma(\omega) = \sigma_0 \sum_j \frac{\lambda_j \tau_j}{4\pi\left(1 + i\left[\omega_{0,j}^2 \frac{\tau_j}{\omega} - \omega\tau_j\right]\right)} \tag{B3}$$

Importantly, we note that Equation B3 collapses to Equation B2 in the limit of no resonances (only one term in the sum) and with $\omega_{0,j} = 0$ and $\tau_j = \tau$.

We can now use Equation B3 to achieve an estimate of the absence of any excited states in the P+ monolayer, given the frequency-independent $\mathrm{Re}[\sigma(\omega)]$ within approximately $\pm 10\%$ (Figure 3). Very simply, this leads to $\left|\frac{\omega_{0,j}^2 \tau_j}{\omega} - \omega\tau_j\right| < 0.1$; assuming $\omega_{max}\tau_j < 0.1$ where $\omega_{max} \approx 2\pi(4\pi\text{GHz})$ is the maximum experimental frequency from Figure 3, we obtain $\omega_{0,j} < \sqrt{0.1\omega_{max}/\tau_j}$. If we then approximate τ_j, as being due to thermal broadening (not intrinsic linewidth of the

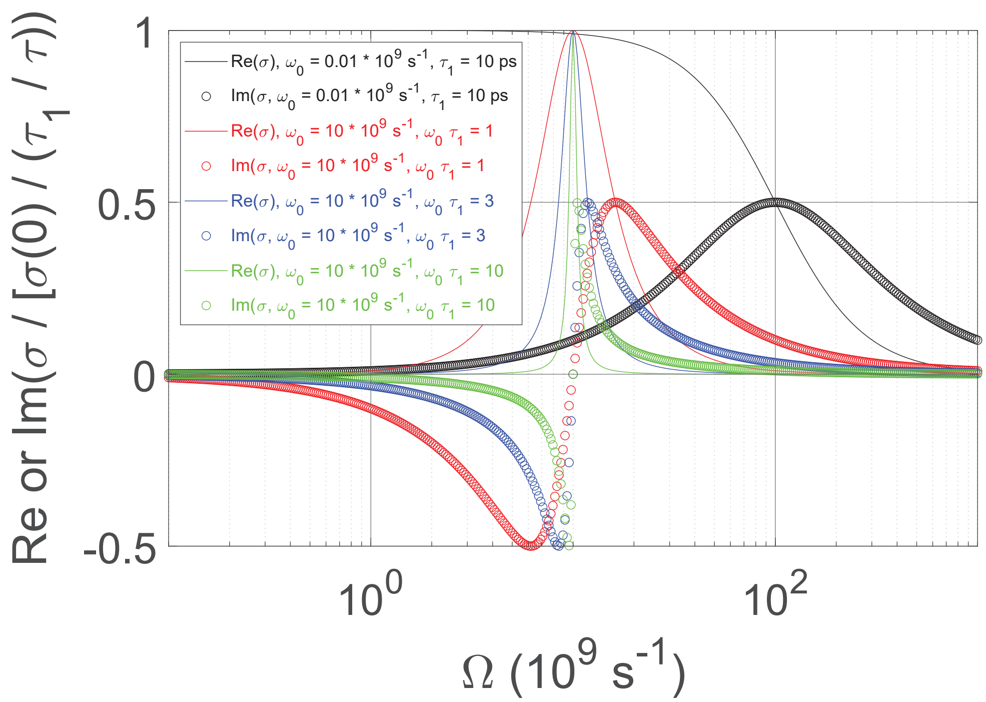

FIG. 7. A few illustrative examples of Equation B3, including (black) a simple Drude result (very small $\omega_{0,1}$) and a variety of single resonances with varying linewidth $\frac{1}{\tau}$.

resonance) at 1 K, we finally obtain a bound on the minimum energy of any resonance of $\hbar\omega_{0,j} < \sqrt{(0.1\frac{\hbar\omega_{max}}{\tau_j/\hbar}} = \sqrt{0.1\hbar\omega_{max}(kT)} \approx 0.1$ meV. Finally, we note that this analysis requires that the possible observation of of conductivity peaks from Equation B3 depends on $\frac{\lambda_j\tau_j}{\lambda\tau}$ being not very small compared to unity; understanding "oscillator strengths" is a complicated topic of its own, and thus a detailed discussion of this assumption is beyond the scope of this paper.

Appendix C: Data Locations

C: \Neil\copy from Elwood 17_3\SET_team\Neil\other peoples documents\Levy\20_5 GHz remote sensing idea manuscript\21_11 P+ experimental paper\figures\22_4 CPW sketch.skp

1. Figure 1

C:\Neil\copy from Elwood 17_3\SET_team\Neil\other peoples documents\Levy\20_5 GHz remote sensing idea manuscript\21_11 P+ experimental paper\figures\22_4 CPW sketch.skp

2. Figure 2

All files in SET_team\Neil\other peoples documents\Levy\20_5 GHz remote sensing idea manuscript\21_11 P+ experimental paper\figures\Fig 2 t raw

'Jun29_25.csv', 'cont', 'continuous CPW'; ... first cooldown

'Jun11_21.csv', 'cont', 'continuous CPW'; ... first cooldown

'Jul16_36.dat', '2_um', '2 um gapped CPW over P^ + monolayer'; ... second cooldown

'Jul16_20.dat', '8_um', '8 um gapped CPW over All files in SET_team\Neil\other peoples documents\Levy\20_5 GHz remote sensing idea manuscript\21_11 P+ experimental paper\figures\Fig 2 t raw

'Jun29_25.csv', 'cont', 'continuous CPW'; ... first cooldown

'Jun11_21.csv', 'cont', 'continuous CPW'; ... first cooldown 'Jul16_36.dat', '2_um', '2 um gapped CPW over P^+ monolayer'; ... second cooldown

'Jul16_20.dat', '8_um', '8 um gapped CPW over P^+ monolayer'; ... second cooldown 'Jun18_46.csv', 'blank_Si', '2 um gapped CPW over blank Si'; ... first cooldown + monolayer'; ... second cooldown

'Jun18_46.csv', 'blank_Si', '2 um gapped CPW over blank Si'; ... first cooldown

3. Figure 3

Value of DC Hall bar resistance: SET_team\Neil\other peoples documents\Levy\20_5 GHz remote sensing idea manuscript\21_11 P+ experimental paper\DC Hall bar results\22_8 Pradeep Data.pptx

Graph: SET_team\Neil\other peoples documents\Levy\20_5 GHz remote sensing idea manuscript\21_11 P+ experimental paper\figures\conductivity\do_plot_P_gapped_CPW_Figure_2.m

and do_calc_save_Converting_Raw_Spectra_to_Conductivity.m

4. Figure 4

SET_team\Neil\other peoples documents\Levy\20_5 GHz remote sensing idea manuscript\21_11 P+ experimental paper\figures\22_1 P+ GHz graphs.pptx

5. Figure 5

SET_team\Neil\other peoples documents\Levy\20_5 GHz remote sensing idea manuscript\21_ 11 P+ experimental paper\figures\23_5 eps files for Antonio\ Fig_5.eps

6. Figure 6

SET_team\Neil\other peoples documents\Levy\20_5 GHz remote sensing idea manuscript\21_11 P+ experimental paper\figures\conductivity\do_Zcouple.m

7. Figure 7

SET_team\Neil\other peoples documents\Levy\20_5 GHz remote sensing idea manuscript\21_11 P+ experimental paper\figures\resonance curves\ do_Drude_resonance.m

[1] J. Wyrick, X. Wang, R. V. Kashid, P. Namboodiri, S. W. Schmucker, J. A. Hagmann, K. Liu, M. D. Stewart Jr, C. A. Richter, G. W. Bryant, and R. M. Silver, "Atom-by-atom fabrication of single and few dopant quantum devices," Advanced Functional Materials **29**, 1903475 (2019).

[2] J. G. Keizer, S. Koelling, P. M. Koenraad, and M. Y. Simmons, "Suppressing segregation in highly phosphorus doped silicon monolayers," ACS nano **9**, 12537–12541 (2015).

[3] J. N. Randall, J. H. Owen, E. Fuchs, J. Lake, J. R. Von Ehr, J. Ballard, and E. Henriksen, "Digital atomic scale fabrication an inverse moore's law–a path to atomically precise manufacturing," Micro and Nano Engineering **1**, 1–14 (2018).

[4] Y. He, S. Gorman, D. Keith, L. Kranz, J. Keizer, and M. Simmons, "A two-qubit gate between phosphorus donor electrons in silicon," Nature **571**, 371–375 (2019).

[5] L. Fricke, S. J. Hile, L. Kranz, Y. Chung, Y. He, P. Pakkiam, M. G. House, J. G. Keizer, and M. Y. Simmons, "Coherent control of a donor-molecule electron spin qubit in silicon," Nature communications **12**, 3323 (2021).

[6] A. L. Levy and N. M. Zimmerman, "Broadband microwave electrical transport spectroscopy for two-dimensional material systems," Journal of Applied Physics **131**, 205102 (2022).

[7] X. Wang, J. A. Hagmann, P. Namboodiri, J. Wyrick, K. Li, R. E. Murray, A. Myers, F. Misenkosen, M. D. Stewart, C. A. Richter, *et al.*, "Quantifying atom-scale dopant movement and electrical activation in si: P monolayers," Nanoscale **10**, 4488–4499 (2018).

[8] V. Dolgopolov, C. Mazure, A. Zrenner, and F. Koch, "Surface conductivity measurements by a capacitive coupling technique," Journal of applied physics **55**, 4280–4283 (1984).

[9] E. Pallecchi, A. C. Betz, J. Chaste, G. Fève, B. Huard, T. Kontos, J.-M. Berroir, and B. Plaçais, "Transport scattering time probed through rf admittance of a graphene capacitor," Phys. Rev. B **83**, 125408 (2011).

[10] A. Inhofer, J. Duffy, M. Boukhicha, E. Bocquillon, J. Palomo, K. Watanabe, T. Taniguchi, I. Esteve, J. Berroir, G. Feve, *et al.*, "rf quantum capacitance of the topological insulator bi 2 se 3 in the bulk depleted regime for field-effect transistors," Physical Review Applied **9**, 024022 (2018).

[11] R. Ulbricht, E. Hendry, J. Shan, T. F. Heinz, and M. Bonn, "Erratum: Carrier dynamics in semiconductors studied with time-resolved terahertz spectroscopy [rev. mod. phys. 83, 543 (2011)]," Rev. Mod. Phys. **89**, 029901 (2017).

[12] N. W. Ashcroft and N. D. Mermin, *Solid state physics* (Holt, Rinehart and Winston, 1976) Chap. Appendix K.